In Situ Amplification and Spatial Mapping of α-Synuclein Seeding Activity

Hengxu Mao[1, #, *], Yaoyun Kuang[1, #], Wei Dai[1], Hao Lin[1], Jinkun Huang[1, *] and Ping-Yi Xu[1, *]

Author affiliations:

1. Dept. of Neurology, the First Affiliated Hospital of Guangzhou Medical University, Guangzhou, 510120, China.

[#]These authors are equally contributing to this work.

***Corresponding to:**

1. Hengxu Mao, Dept. of Neurology, the First Affiliated Hospital of Guangzhou Medical University, Guangzhou, 510120, China. Email address: hengxu2010@qq.com.
2. Jinkun Huang, Dept. of Neurology, the First Affiliated Hospital of Guangzhou Medical University, Guangzhou, 510120, China. Email address: 2009681002@gzhmu.edu.cn.
3. Ping-Yi Xu, Dept. of Neurology, the First Affiliated Hospital of Guangzhou Medical University, Guangzhou, 510120, China. Email address: pingyixu@sina.com.

Abstract

The prion-like propagation of proteopathic α-synuclein (αSyn) "seeds" is a central pathogenic mechanism in synucleinopathies. However, methods to directly visualize this "seeding activity" within intact tissue are lacking. Conventional antibody-based techniques provide only static snapshots of pathological deposits, while sensitive seed amplification assays lose spatial information via mechanical fragmentation. Here, we introduce the αSyn Quiescent Seed Amplification Assay (QSAA), a method for specific, robust, in situ amplification of

αSyn seeds directly within tissue sections. QSAA demonstrates superior sensitivity and earlier detection than pS129 and ThS staining, revealing widespread seeding in a PD mouse model, and successfully identifies endogenous seeds in archival human brains. By integrating with immunofluorescence, IF-QSAA uncovered microglial seeding activity and established that pS129 phosphorylation and seeding activity represent distinct pathological states. This offers unprecedented spatial insights into synucleinopathy pathogenesis, holding significant promises for early diagnosis and therapeutic evaluation.

Keywords: α-Synuclein, Seed amplification assay, Quiescent SAA, Parkinson's disease, Seeding activity

Introduction

Synucleinopathies, including Parkinson's disease (PD), dementia with Lewy bodies (DLB), and multiple system atrophy (MSA), are progressive neurodegenerative disorders defined by the pathological accumulation of α-synuclein (αSyn) [1,2]. In these diseases, αSyn misfolds into proteopathic seeds capable of self-propagation through a prion-like mechanism, templating the conversion of native αSyn into insoluble aggregates[3,4]. This functional property, termed seeding activity, is a primary driver of pathology progression, leading to widespread neuronal dysfunction and neurodegeneration[5,6]. Consequently, visualizing the spatiotemporal distribution and propagation pathways of αSyn seeding activity is critical for understanding synucleinopathy pathogenesis and developing targeted therapies.

Conventional antibody-based techniques, which often target pathological markers like αSyn phosphorylated at Serine 129 (pS129), have been invaluable in localizing αSyn aggregates in diseased brains[7,8]. However, these methods provide only a static snapshot of aggregate presence and fail to capture the dynamic seeding activity that underpins pathology[9-12]. To bridge this gap, seed amplification assays (SAAs) have been developed, exploiting the

inherent ability of misfolded αSyn seeds to induce amplification in vitro by recruiting exogenous monomeric substrates[13,14]. Despite their high sensitivity, traditional SAAs depend on tissue homogenization and mechanical fragmentation (e.g., shaking or sonication) to sustain the amplification reaction[15,16]. This process disrupts tissue architecture and abolishes spatial information about seed localization.

To address these challenges, we developed the αSyn Quiescent Seed Amplification Assay (QSAA), a method that enables in situ amplification of αSyn seeds within tissue sections without mechanical fragmentation. By optimizing reaction conditions, including the introduction of sulfate ions (SO_4^{2-}), elevating temperature to 70°C, and using mouse-derived αSyn monomers as the substrate, QSAA achieves seed-dependent fibril elongation under quiescent conditions. This approach preserves spatial context and generates high-resolution propagation maps, revealing pathological spread patterns inaccessible by antibody staining alone. QSAA is compatible with a variety of samples, demonstrating broad applicability by successfully detecting endogenous seeds in human brain sections, including long-term formalin-fixed archival specimens. Furthermore, by integrating QSAA with immunofluorescence (IF), IF-QSAA can simultaneously visualize amplified seeds and specific cellular markers. This dual-labeling approach provides a comprehensive, cellular-level view of αSyn seeding activity, offering new insights into the mechanisms of synucleinopathies. Together, QSAA and IF-QSAA represent powerful tools to advance our understanding of αSyn propagation, holding great promise for improving diagnosis and therapeutic development.

Results

Development of a quiescent system for αSyn seed amplification

A key prerequisite for in situ amplification of αSyn seeds is the ability to achieve robust and

70 specific amplification under quiescent conditions. Traditional SAAs primarily rely on cyclic
71 physical fragmentation to continuously generate new growth ends from fibrils that have
72 entered the reaction plateau[17,18], thereby sustaining rapid amplification (**Fig. 1a, solid line**).
73 In contrast, a quiescent system necessitates an alternative mechanism to maintain high
74 amplification efficiency (**Fig. 1a, dashed line**). To address this, our strategy focused on
75 optimizing the biochemical environment to intrinsically accelerate fibril amplification in a
76 seed-dependent manner, thereby circumventing the need for physical fragmentation (**Fig. 1b**).

77 We systematically examined several factors known to affect αSyn fibril growth,
78 including the αSyn monomer substrate[13,19,20], chemical additives[21-24], and incubation
79 temperature[25,26]. Initially, we constructed expression plasmids for human wild-type (hWT),
80 human A53T mutant (hA53T), and mouse wild-type (mWT) αSyn, confirming their
81 sequences (**Fig. 1c**). Notably, mWT αSyn naturally contains a threonine at position 53,
82 analogous to the pathogenic A53T mutation in humans, which is known to accelerate αSyn
83 aggregation[27]. Consistent with this, we demonstrated a progressively faster aggregation rate
84 from hWT to hA53T and then to mWT, confirming that mWT αSyn serves as a more
85 aggregation-prone substrate suitable for rapid amplification. Next, we explored the impact of
86 additives and temperature on fibril amplification. Previous studies have shown that sulfate
87 ions (SO_4^{2-}) can promote αSyn fibril elongation by electrostatically stabilizing misfolded
88 aggregates[21,22] and that an elevated temperature accelerates aggregation kinetics[25,26]. We
89 evaluated these parameters individually to establish their baseline effects in the presence of
90 αSyn pre-formed fibrils (PFFs) under cyclic fragmentation conditions (**Fig. 1d**). Each
91 parameter (mWT αSyn monomer, SO_4^{2-}, 70°C) independently shortened the lag phase of
92 αSyn seed amplification (**Fig. 1e**). However, combining these factors under cyclic
93 fragmentation resulted in rapid spontaneous amplification, leading to poor specificity (**Fig.
94 1f**). Remarkably, applying the same combination (mWT αSyn monomer, SO_4^{2-}, 70°C) under

95 quiescent conditions yielded rapid and specific amplification with a high fold separation of
96 7.547 (**Fig. 1g**). These results underscore that the optimized chemical environment and
97 elevated temperature in QSAA effectively compensate for the lack of mechanical
98 fragmentation, enabling continuous and robust fibril growth from existing seeds while
99 minimizing spontaneous nucleation.

100 To further characterize the amplification products, we performed Transmission Electron
101 Microscopy (TEM) on samples generated by QSAA (**Fig. 1h**). TEM analysis revealed
102 fibrillar morphologies characteristic of αSyn aggregates, including both densely packed and
103 loosely associated fibrillar assemblies. In contrast, no fibrillar products were observed in the
104 unseeded group, further demonstrating the specificity of the assay (**Fig. 1h**, Inset).

105 **QSAA Enables In Situ Amplification and Mapping of αSyn Seeding Activity in Brain**
106 **Sections**

107 Having established a quiescent amplification system, we sought to expand its application for
108 in situ amplification on brain tissue sections. We developed a standardized operating
109 procedure (SOP) involving tissue fixation, dehydration, sectioning, post-fixation, and
110 incubation with the QSAA reaction buffer (**Fig. 2a**). To minimize artifacts caused by
111 microscale fluid movement, a semi-solid agarose membrane was overlaid on the tissue
112 sections during incubation[28].

113 Brain sections from a synucleinopathy mouse model[29,30] at 180 days post-injection (dpi)
114 of mouse αSyn pre-formed fibrils (mPFFs) revealed widespread αSyn seeding activity after 5
115 hours of incubation (**Fig. 2b**). The signal propagated along neuroanatomical tracts, such as
116 the bilateral corpus callosum (CC) and anterior commissure (AC), into the contralateral
117 hemisphere, whereas control sections from PBS-injected mice were negative (**Fig. 2b, Inset**).
118 This pattern, consistently observed across coronal, sagittal, and horizontal sections,

effectively mapped pathology routes directly within the tissue, with sagittal views clearly showing dissemination along the anterior commissure's olfactory limb (ACO) towards the olfactory bulb (OB) (**Fig. 2b, sagittal**).

To confirm the Thioflavin T (ThT) signal represented seed-dependent fibril formation, we used TEM on QSAA-treated tissue, which revealed typical αSyn amyloid fibrils within the tissue interstitium and on its surface (**Fig. 2c**). Brightfield microscopy further showed that fluorescent signals precisely co-localized with macroscopic aggregates, confirming that tangible amplification products were generated (**Fig. 2d**). These observations validate that QSAA amplifies αSyn seeds within intact tissue architecture.

QSAA Provides Superior Sensitivity and Early Detection of αSyn Pathology

By leveraging the ability of QSAA to preserve spatial information, we generated a brain-wide map of αSyn seeding activity in mPFF-injected mice (180 dpi) and compared it with pS129-αSyn immunofluorescence on consecutive sections (**Fig. 3a**). QSAA and pS129 signals showed broad concordance across multiple brain regions, including the striatum (STR), primary and secondary motor cortex (M1/M2), secondary somatosensory cortex (S2), and entorhinal cortex (ECT), confirming that QSAA faithfully localizes pathological seeds. Importantly, QSAA revealed a much wider pathological landscape, particularly within white matter tracts such as the bilateral corpus callosum (CC), anterior commissure (ACA/ACP), ipsilateral internal capsule (IC), external capsule (EC), medial forebrain bundle (MFB), fasciculus retroflexus (FR), and nigrostriatal tract (NST). In these regions, pS129 immunoreactivity was relatively sparse, likely reflecting the lower density of neuronal soma.

To further demonstrate the sensitivity of QSAA, we compared QSAA, pS129-IF, and Thioflavin S (ThS) staining on sections from mice injected with one-tenth the standard dose of mPFFs and analyzed at 30 dpi (**Fig. 3b**). QSAA revealed widespread fluorescent signals

143 across the cortex, corpus callosum, and striatum of both hemispheres, whereas pS129
144 detected only sparse, neuritic-like structures, and ThS staining showed even weaker signals
145 (**Fig. 3c**).

146 We next examined the ability of QSAA to detect early-stage pathology. Because QSAA
147 directly amplifies functional seeding activity rather than depending on downstream
148 phosphorylation events, it confers a mechanistic advantage over pS129 immunostaining.
149 Remarkably, QSAA detected distinct seeding activity as early as 7 dpi, a stage at which
150 pS129 signals were undetectable (**Fig. 3d**). By 14 dpi, QSAA revealed widespread
151 dissemination of αSyn seeding throughout the brain, whereas pS129 immunoreactivity was
152 only beginning to emerge. Whole-brain QSAA mapping at 14 dpi confirmed broad
153 propagation of seeding activity beyond the injection site, with no signal observed in PBS-
154 injected controls (**Fig. 3e**). These findings demonstrate that extensive αSyn seeding precedes
155 the detectable onset of pS129 pathology in the exogenous seeding model.

156 **QSAA is Applicable to Endogenous Seeds in Human Brain Tissue**

157 We next evaluated the applicability of QSAA to detect endogenous αSyn seeds in postmortem
158 human brain tissue. Striatal sections from patients with PD, progressive supranuclear palsy
159 (PSP), and healthy controls (HC) were analyzed. QSAA generated ThT fluorescence
160 selectively in PD brains, with no signal observed in HC or PSP samples, demonstrating high
161 specificity (**Fig. 4a**). Notably, QSAA was able to detect seeding activity in PD specimens that
162 had been fixed in formalin for more than 20 years, in which pS129-IF failed to detect
163 pathology (**Fig. 4a, FF-PD**). This finding indicates the stability of seeding-competent αSyn
164 aggregates compared with antibody epitopes that deteriorate during prolonged fixation. To
165 validate these results independently, we performed Real-Time Quaking-Induced Conversion
166 (RT-QuIC) on lysates from the same brain specimens, which confirmed the seeding activity

167 in both frozen and formalin-fixed PD samples (**Fig. 4b-c**).

168 QSAA further revealed distinct spatial distributions of seeding activity in human PD
169 brains (**Fig. 4d**). Seeding was detected predominantly in gray matter regions such as the
170 striatum and cortex, whereas the corpus callosum showed no detectable activity (**Fig. 4e**).
171 This contrasts with the mPFF-inoculated mouse model, where seeding also occurs within
172 white matter tracts, suggesting differences in propagation dynamics between exogenously
173 induced pathology and endogenously developed diseases. Finally, a time-course analysis of
174 QSAA on PD brain sections revealed a clear, time-dependent increase in ThT fluorescence
175 intensity at defined sites of αSyn seeding (**Fig. 4f**). Signals appeared as early as 1 h and
176 continued to amplify through 5 h, highlighting both the sensitivity of the method and its
177 ability to dynamically monitor in situ seeding activity.

178 **IF-QSAA Reveals Distinct Cellular Localization and Complementary Pathological**
179 **States of Seeding Activity and pS129**

180 We developed an integrated immunofluorescence-QSAA (IF-QSAA) protocol to determine
181 the cellular localization of αSyn seeding activity. First, we confirmed the spectral
182 compatibility of ThT with common IF fluorophores, finding that its excitation spectrum is
183 distinct from DAPI, Cy3, and Cy5, but overlaps significantly with FITC (**Fig. 5a**). Next, a
184 sequential optimization revealed that the QSAA reaction conditions (70°C, SO_4^{2-}, 5h)
185 degraded antibody epitopes, necessitating an "IF-first" workflow to preserve both signals
186 (**Fig. 5b**). Applying this protocol with confocal microscopy on brain tissue from mPFF-
187 injected mice (180 dpi), we visualized intraneuronal QSAA products (**Fig. 5c, arrows**) and
188 larger products extending into the extracellular space (**Fig. 5c, arrowheads**). These results
189 validated the capability of IF-QSAA to map seeding activity with subcellular precision,
190 leading to our standardized IF-QSAA protocol **(Fig. 5d**).

To identify the specific cell types involved in αSyn seeding, we co-labeled sections from mPFF-injected mice (30 dpi) with markers for neurons (NeuN), microglia (IBA1), and astrocytes (GFAP). Strikingly, in addition to neuronal signals (**Fig. 5e**), we observed extensive co-localization between QSAA signals and IBA1-positive microglia (**Fig. 5f**), but not with GFAP-positive astrocytes (**Fig. 5g**). This finding contrasted with the cellular distribution of pS129-αSyn pathology[31], which was predominantly found within neurons (**Fig. 5h**) and showed minimal co-localization with microglia (**Fig. 5i**). These findings suggest a previously underappreciated role for microglia in the uptake, processing, or propagation of αSyn seed species, differing from the traditional view that Lewy pathology primarily accumulates within neurons.

To further investigate the relationship between αSyn seeding activity and pS129 pathology, we applied IF-QSAA to brain tissue sections from the mPFF mouse model. Through simultaneous imaging of the QSAA signal and pS129, we observed a heterogeneity among αSyn aggregates, with multiple subtypes coexisting in the same microspatial environment (**Fig. 5j**). Initially, we identified a large population of aggregates positive for both signals (QSAA+/pS129+), which exhibited a characteristic "core-halo" structure, comprising a dense, pS129-positive core enveloped by a more diffuse QSAA signal halo. This finding suggested that phosphorylated αSyn with seeding capacity is a significant component of the pathological landscape. However, this observation raises a critical question: is pS129 a reliable surrogate for αSyn seeding activity? A closer examination of the magnified regions in Figure 5j revealed that, in addition to the dual-positive aggregates, we could also identify: 1) aggregates that were exclusively pS129-positive but QSAA-negative (QSAA−/pS129+), appearing as discrete red puncta; and 2) aggregates that were exclusively QSAA-positive but pS129-negative (QSAA+/pS129−), appearing as distinct green puncta. This direct visual evidence demonstrates that αSyn seeding activity and its pS129

phosphorylation state are not strictly concordant or co-localized (**Fig. 5k**).

We therefore propose a "four-quadrant model" to classify αSyn aggregates (**Fig. 5l**): QSAA+/pS129+ (Co-existent): Phosphorylated aggregates with seeding capacity, forming the characteristic core-halo structure. QSAA+/pS129− (Seeding-Dominant): Aggregates possessing seeding activity but with pS129 levels below the detection threshold or with a masked epitope. QSAA−/pS129+ (Phosphorylation-Dominant): Phosphorylated aggregates that have either lost or inherently lack seeding competency. QSAA−/pS129− (Pathology-Free): Regions devoid of detectable seeding activity and pS129 pathology. This model emphasizes that αSyn seeding activity and pS129 immunoreactivity represent two distinct yet complementary pathological states, rather than being equivalent disease markers. It provides a more precise framework for understanding the molecular heterogeneity and microenvironmental complexity of αSyn pathology in synucleinopathies.

Discussion

In this study, we established QSAA, a method that enables the in situ detection of αSyn seeding activity. Unlike antibody-based methods that capture pre-formed aggregates[32], or conventional SAAs that require tissue homogenization[33,34], QSAA achieves rapid, seed-dependent amplification under quiescent conditions. This methodology allows for the direct visualization of functional seeding activity within intact tissue sections.

QSAA provided several key insights that extend beyond the capabilities of existing techniques. First, its amplification-based nature provided markedly superior sensitivity, enabling the detection of nascent αSyn seeds. Second, QSAA revealed a broader pathological landscape, particularly within white matter tracts and microglial populations, where antibody-based methods are often less effective. This is likely because conventional antibodies targeting post-translational modifications (PTMs) like pS129 rely on late-stage pathological

events[9,11], giving QSAA a distinct advantage in detecting seeding species that are either unmodified or at very early stages of aggregation. Together with the IF-QSAA protocol, these findings led us to propose a conceptual "four-quadrant model," in which seeding activity and pS129 phosphorylation define both overlapping and distinct dimensions of αSyn pathology. This framework highlights early-stage QSAA+/pS129− seeds as a potentially critical driver of disease progression that is not captured by conventional markers. Importantly, QSAA also demonstrated strong translational potential. It successfully amplified endogenous seeds from postmortem PD brains, including archival tissue fixed for over 20 years, where pS129 immunoreactivity had deteriorated. This underscores the remarkable stability of seeding-competent αSyn structures and positions QSAA as a promising tool for both retrospective neuropathological studies and diagnostic applications.

While QSAA offers the unique advantage of in situ assessment, it currently cannot differentiate between distinct αSyn strains, a property reported for some conventional SAAs[35-37], nor can it directly identify PTMs as antibody-based methods can[38,39]. Future methodological refinements, such as fluorescence-based conformational fingerprinting of amplified fibrils[40] or the engineering of strain-specific monomer substrates, may broaden its utility.

Although the high sensitivity of QSAA arises from controlled, seed-dependent amplification rather than from non-specific background signals, the risk of experimental false positives still requires rigorous control. Despite multiple layers of mitigation strategies including an agarose overlay, strict incubation time, parallel negative samples, and in situ TEM validation, further standardization will be essential for multi-center implementation. Uniform parameters such as section thickness, fixation protocols, and data normalization will be critical for ensuring inter-laboratory reproducibility[17].

In conclusion, QSAA provides a powerful platform for mapping αSyn seeding activity in situ with high sensitivity and specificity. By extending beyond static aggregate detection to capture the functional and spatial dimensions of pathogenic seeds, QSAA deepens our understanding of synucleinopathy pathogenesis and holds promise for clinical applications in early diagnosis and therapeutic evaluation. Moreover, the principle of quiescent amplification may be adaptable to other misfolded proteins, such as Tau and TDP-43, particularly those that have already demonstrated cyclic fragmentation-based amplification in vitro[41,42], further broadening its relevance to neurodegenerative disease research.

Methods

Ethics and Oversight

All animal procedures were conducted in strict accordance with the guidelines established by the Institutional Animal Care and Use Committee of Guangzhou Medical University. Human brain tissues were obtained from the Department of Neurology, First Affiliated Hospital of Guangzhou Medical University, with written informed consent from the next of kin and approval from the hospital Ethics Committee (MRE. No. 155). All experiments complied with relevant ethical regulations.

Animals and Stereotaxic Injections

Male C57BL/6J mice (10-12 weeks old, RRID: IMSR_JAX:000664) were purchased from the Experimental Animal Center of Guangzhou Medical University. Animals were maintained in a SPF facility on a 12-h light/dark cycle with ad libitum access to food and water. Sample size was chosen based on previous studies using similar models to ensure sufficient power for detecting inter-group differences. Animals were randomly assigned to experimental groups. All injections, data acquisition, and subsequent analyses were performed by experimenters blinded to the treatment conditions

For stereotaxic surgery, mice were anesthetized with isoflurane (2.5% for induction, 1.5% for maintenance) and placed in a stereotaxic frame (Kopf Instruments, Model 940). Recombinant mouse αSyn pre-formed fibrils (mPFFs; 5 μg in 1 μL) or an equal volume of sterile PBS were injected unilaterally into the right striatum. Coordinates were determined relative to bregma according to the Paxinos & Franklin mouse brain atlas (3rd edition): AP: +0.8 mm, ML: +2.0 mm, DV: -3.5 mm. Injections were performed using a 10-μL Hamilton syringe with a 33-gauge needle connected to a microinfusion pump at a rate of 0.2 μL/min. The needle was left in place for 10 min post-injection to minimize backflow before being

297 slowly withdrawn. For the low-dose sensitivity comparison, a one-tenth dose of mPFFs (0.5
298 μg in 1 μL) was used. At specified time points (7, 10, 14, 30, or 180 days post-injection),
299 mice were deeply anesthetized and transcardially perfused with ice-cold PBS followed by 4%
300 (w/v) paraformaldehyde (PFA) in 0.1 M phosphate buffer (PB, pH 7.4). Brains were post-
301 fixed in the same fixative for 24 h at 4°C, then cryoprotected in 30% (w/v) sucrose in PBS
302 until sectioning.

303 **Human Brain Specimens**

304 Postmortem human brain tissues (collected 2005-2022) were obtained from the First
305 Affiliated Hospital of Guangzhou Medical University. The cohort included pathologically
306 confirmed cases of Parkinson's disease (PD; n=3), progressive supranuclear palsy (PSP; n=3),
307 and age-matched healthy controls with no history of neurological disease (HC; n=3).
308 Diagnoses were established postmortem based on consensus neuropathological criteria,
309 including Braak staging for Lewy body pathology. The postmortem interval (PMI) for all
310 fresh-frozen and standard-fixed samples was <12 h. For each case, the left hemisphere was
311 fixed in 10% neutral buffered formalin (NBF) for 2-4 weeks, while the right hemisphere was
312 coronally sliced and snap-frozen at -80°C. Along-term fixed PD specimen (FF-PD) had been
313 stored in 10% NBF for over 20 years at room temperature.

314 **α-Synuclein Monomer Expression and PFF Preparation/QC**

315 Recombinant full-length mouse wild-type α-synuclein (mWT, UniProt ID: P58992) was
316 expressed in *E. coli* BL21 (DE3) cells (TransGen Biotech, CD601) and purified as previously
317 described with modifications[43,44]. Following IPTG induction (1 mM, 4 h), cells were lysed by
318 sonication in high-salt buffer (10 mM Tris-HCl, pH 7.5, 500 mM NaCl, 1 mM EDTA, 1 mM
319 PMSF, and 1x Protease inhibitor). The lysate was boiled for 15 min, followed by 45%
320 ammonium sulfate precipitation and pH 3.0 acid precipitation. Endotoxin was removed using

321 a high-capacity endotoxin removal resin (Sangon Biotech, B641718). The protein was further
322 purified by anion exchange chromatography (HiTrap Q HP column, Cytiva, 17115401). The
323 final monomer was dialyzed against TBS (10mM Tris-HCl pH 7.5, 50mM NaCl), filtered
324 through a 50-kDa cutoff filter (Amicon Ultra), and stored at -80°C.

325 To generate mPFFs, monomeric mouse αSyn (5 mg/mL in PBS) was incubated at 37°C
326 with continuous agitation (1000 rpm) in an Eppendorf ThermoMixer C for 7 days. The
327 resulting fibril suspension was fragmented into seeds using a non-contact water-bath
328 sonicator (SCIENTZ, SCIENTZ08-III) for a total of 5 min using 300 pulses of 1-s on/1-s off
329 at 90% power. PFF quality control was performed for each batch[45]. TEM confirmed fibrillar
330 morphology. Dynamic light scattering (DLS) confirmed an average hydrodynamic diameter
331 of 50-150 nm. Functional activity was validated using a standard SAA, with each batch
332 required to produce a lag time within ±15% of a reference standard batch when seeded with 1
333 pg of PFFs.

334 **Plate-based Seed Amplification Assays**

335 Agitated SAA: Reactions were prepared in a 96-well black, clear-bottom plate (Thermo
336 Scientific, 165305) in a final volume of 100 μL. Each well contained 1 mg/mL m-αSyn
337 monomer, 40 μM Thioflavin T (ThT), and 1 pg PFFs (or PBS for no-seed controls) in
338 Agitation Buffer (10 mM NaCl, 10 mM Tris-HCl, pH 7.5). Where indicated, 800 mM Na_2SO_4
339 was added. The plate was sealed with an optical adhesive film (Applied Biosystems,
340 4311971) and incubated in a plate reader (SpectraMax iD5, Molecular Devices) at 37°C. A
341 cycle of 1 min orbital shaking (700 rpm, double orbital) followed by 14 min of rest was
342 repeated. ThT fluorescence was measured every 15 min (Ex: 450 nm, Em: 490 nm, bottom-
343 read).

344 Quiescent SAA: Reactions were prepared in a 96-well polypropylene PCR plate

(Thermo Scientific, AB0700) in a final volume of 20 μL. Each reaction contained 1 mg/mL mWT-αSyn monomer and 40 μM ThT in QSAA Reaction Buffer (800 mM Na_2SO_4, 25 mM NaCl, 10mM Tris-HCl, pH 6.0), seeded with 1 pg mPFFs or TBS. Each reaction was overlaid with 20 μL of mineral oil (Biosharp, BS927) to prevent evaporation. The plate was sealed and incubated in a real-time PCR instrument (Bio-Rad, CFX96) at 70°C without agitation. ThT fluorescence was monitored every 30 min via the FAM channel (Ex: 452-486 nm, Em: 505-545 nm). Lag phase was defined as the time to cross a threshold of the mean baseline fluorescence plus five standard deviations.

In Situ QSAA on Tissue Sections

Brains were sectioned at 14 μm thickness onto high-adhesion glass slides (CITOTEST, 188105W). Sections were air-dried for 30 min, then post-fixed in ice-cold acetone for 10 min at -20°C and air-dried again. For FF-PD tissues, 95°C PBS treatment for 1 h was performed prior to sectioning to reverse formalin cross-linking and restore seeding activity. To perform QSAA, a reaction mix was prepared containing 1 mg/mL m-αSyn monomer, 40 μM ThT in Reaction Buffer (800 mM Na_2SO_4, 25 mM NaCl, 10 mM Tris-HCl, pH 6.0). To prevent micro-convection and ensure even reagent distribution, a pre-warmed (~50 °C) 1% (w/v) agarose solution (in ddH_2O) was overlaid onto the tissue section to form a gel approximately 1 mm thick. After gelling at room temperature (~5min), the agarose was carefully trimmed flush with the tissue edges using a scalpel. Subsequently, 300 μL of the reaction mix was added to cover each section. The slide was then placed in a humidified, sealed chamber on a temperature-controlled stage (Ruicheng Instrument Co., TS400) and incubated at 70°C for 0-12 h unless otherwise specified. Following incubation, the agarose film was gently removed by immersing the slide in heated (95 °C) PBS, and the slide was washed 3 times for 1 min each in PBS before mounting with a coverslip.

369 **IF-QSAA Workflow**

370 An "IF-first" protocol was implemented to preserve antibody epitopes, which were found to
371 be sensitive to the 70°C incubation. Sections were first processed for standard
372 immunofluorescence. Briefly, sections were permeabilized with 0.5% Triton X-100 in PBS
373 for 15 min and blocked with 5% normal goat serum in PBS for 1 h at room temperature.
374 Primary antibodies (see Table 1 for details) were diluted in blocking buffer and incubated
375 overnight at 4°C. After washing, sections were incubated with corresponding Alexa Fluor-
376 conjugated secondary antibodies (1:1000, Invitrogen) for 1 h at room temperature. Following
377 IF, sections were washed thoroughly in PBS and then subjected to the In Situ QSAA protocol
378 as described above.

379 **Thioflavin S Staining**

380 Sections were incubated in 0.05% ThS in 50% ethanol for 8 min, differentiated in 80%
381 ethanol, and treated with TrueBlack® Lipofuscin Autofluorescence Quencher (Biotium,
382 23007) to suppress background fluorescence. After rinsing in PBS, slides were coverslipped
383 with aqueous mounting medium and imaged.

384 **Microscopy and Image Quantification**

385 Fluorescence images were acquired using a NIKON ECLIPSE Ti2-E microscope equipped
386 with a 4×, 10×, and 20× objectives. High-resolution confocal images were acquired on a
387 Leica SP8 scanning confocal microscope using a 40× (NA 0.75) or a 63× oil-immersion (NA
388 1.40) objective. To prevent spectral bleed-through, a sequential scanning strategy was
389 employed, acquiring signals in descending order of emission wavelength: Cy5/Alexa Fluor
390 647 (Ex: 633 nm, Em: 650-720 nm) → Cy3/Alexa Fluor555 (Ex: 561 nm, Em: 570-630 nm)
391 → ThT/QSAA (Ex: 488 nm, Em: 495-550 nm) →DAPI (Ex: 405 nm, Em: 415-470 nm).
392 Notably, because ThT emission (not excitation spectra) partially overlaps with DAPI,

subtraction or spectral unmixing was applied during analysis. Z-stacks were acquired with a 2 μm step size over a 50 μm range.

All images intended for comparison were acquired using identical microscope settings (laser power, gain, offset) and processed with the same linear adjustments for brightness and contrast. Image analysis was performed using Fiji/ImageJ (v2.3.0). For quantification of fluorescence intensity, regions of interest were manually drawn, and the mean gray value was measured. All experiments were performed with at least three independent biological replicates.

Transmission Electron Microscopy

For solution-state products, 10 μL of QSAA reaction mixture was adsorbed onto glow-discharged, 400-mesh carbon-coated copper grids for 2 min, washed with ddH_2O, and negatively stained with 2% (w/v) uranyl acetate. For in situ products, QSAA-treated tissue sections were scraped from the slide, fixed in 2.5% glutaraldehyde/2% PFA in 0.1 M cacodylate buffer, post-fixed with 1% osmium tetroxide, dehydrated in ethanol, and embedded in EMBed 812 resin. Ultrathin sections (70 nm) were cut, placed on grids, and stained with uranyl acetate and lead citrate. All grids were imaged on a FEI Talos L120C TEM at 120 kV.

RT-QuIC Validation

Brain homogenates (10% w/v) from human samples were prepared in ice-cold PBS using a bead beater. Homogenates were serially diluted from 10^{-2} to 10^{-5} in PBS. RT-QuIC reactions were set up in a 96-well plate with each well containing 100 μL of reaction mix: 0.1 mg/mL human αSyn (1-140), 10 μM ThT, 10 mM Tris (pH 7.5), and 50 mM NaCl. 2 μL of diluted brain homogenate was added to seed the reactions. The plate was incubated in a BMG FLUOstar Omega plate reader at 37°C with cycles of 1 min shaking (700 rpm, double orbital)

and 1 min rest. ThT fluorescence (Ex: 450 nm, Em: 490 nm) was recorded every 15 min. A sample was considered positive if the fluorescence of at least two of three technical replicates crossed a threshold calculated as the mean of negative control wells plus five standard deviations.

Statistical Analysis

All statistical analyses were performed using GraphPad Prism (v9.0). Data are presented as mean ± SD unless otherwise noted. Before applying parametric tests, data were assessed for normality using the Shapiro-Wilk test and for homogeneity of variances using Levene's test. Comparisons between two groups were performed using a two-tailed, unpaired Student's t-test. Comparisons among three or more groups were performed using one-way ANOVA followed by Tukey's post hoc test for multiple comparisons. For data involving two independent variables, a two-way ANOVA with Tukey's multiple comparisons test was used. A P value < 0.05 was considered statistically significant. Specific statistical details for each experiment, including the exact value of n and what n represents, are provided in the figure legends.

Data availability

Any additional information required to reanalyze the data reported in this report is available from the corresponding author upon reasonable request. All materials used in this study will be made available subject to a materials transfer agreement (MTA). This paper does not report the original code.

Acknowledgments

This work was supported by grants from the National Natural Science Foundation of China (grant numbers 81870856, 81870992, and 32171236).

Author contributions

H.M. designed the study, performed experiments, and wrote the manuscript. Y.K. supervised experiments, analyzed data, and contributed to manuscript preparation. D.W. and H.L. assisted with experimental procedures and data collection. H.M., J.H., and P-Y.X. provided project oversight, funding, and critical revisions to the manuscript.

Competing interests

The authors declare that they have no competing interests.

References

1 Schweighauser, M. *et al.* Structures of alpha-synuclein filaments from multiple system atrophy. *Nature* **585**, 464–469 (2020). https://doi.org/10.1038/s41586-020-2317-6

2 Yang, Y. *et al.* Structures of alpha-synuclein filaments from human brains with Lewy pathology. *Nature* **610**, 791–795 (2022). https://doi.org/10.1038/s41586-022-05319-3

3 Rodriguez, J. A. *et al.* Structure of the toxic core of alpha-synuclein from invisible crystals. *Nature* **525**, 486–490 (2015). https://doi.org/10.1038/nature15368

4 Theillet, F. X. *et al.* Structural disorder of monomeric alpha-synuclein persists in mammalian cells. *Nature* **530**, 45–50 (2016). https://doi.org/10.1038/nature16531

5 Volpicelli-Daley, L. A. *et al.* Exogenous alpha-synuclein fibrils induce Lewy body pathology leading to synaptic dysfunction and neuron death. *Neuron* **72**, 57–71 (2011). https://doi.org/10.1016/j.neuron.2011.08.033

6 Thomzig, A. *et al.* Transmissible alpha-synuclein seeding activity in brain and stomach of patients with Parkinson's disease. *Acta Neuropathol* **141**, 861–879 (2021). https://doi.org/10.1007/s00401-021-02312-4

7 Anderson, J. P. *et al.* Phosphorylation of Ser-129 is the dominant pathological modification of alpha-synuclein in familial and sporadic Lewy body disease. *J Biol Chem* **281**, 29739–29752 (2006). https://doi.org/10.1074/jbc.M600933200

8 Fujiwara, H. *et al.* alpha-Synuclein is phosphorylated in synucleinopathy lesions. *Nat Cell Biol* **4**, 160–164 (2002). https://doi.org/10.1038/ncb748

9 Mahul-Mellier, A. L. *et al.* The process of Lewy body formation, rather than simply alpha-synuclein fibrillization, is one of the major drivers of neurodegeneration. *Proc Natl Acad Sci U S A* **117**, 4971–4982 (2020). https://doi.org/10.1073/pnas.1913904117

10 Lashuel, H. A. *et al.* Revisiting the specificity and ability of phospho-S129 antibodies to capture alpha-synuclein biochemical and pathological diversity. *NPJ Parkinsons Dis* **8**, 136 (2022). https://doi.org/10.1038/s41531-022-00388-7

11 Ghanem, S. S. *et al.* alpha-Synuclein phosphorylation at serine 129 occurs after initial protein deposition and inhibits seeded fibril formation and toxicity. *Proc Natl Acad Sci U S A* **119**, e2109617119 (2022). https://doi.org/10.1073/pnas.2109617119

12 Ramalingam, N. *et al.* Dynamic physiological alpha-synuclein S129 phosphorylation is driven by neuronal activity. *NPJ Parkinsons Dis* **9**, 4 (2023). https://doi.org/10.1038/s41531-023-00444-w

13 Groveman, B. R. *et al.* Rapid and ultra-sensitive quantitation of disease-associated alpha-synuclein seeds in brain and cerebrospinal fluid by alphaSyn RT-QuIC. *Acta Neuropathol Commun* **6**, 7 (2018). https://doi.org/10.1186/s40478-018-0508-2

14 Shahnawaz, M. *et al.* Development of a Biochemical Diagnosis of Parkinson Disease by Detection of alpha-Synuclein Misfolded Aggregates in Cerebrospinal Fluid. *JAMA Neurol* **74**, 163–172 (2017). https://doi.org/10.1001/jamaneurol.2016.4547

15 Soto, C., Saborio, G. P. & Anderes, L. Cyclic amplification of protein misfolding: application to prion-related disorders and beyond. *Trends Neurosci* **25**, 390–394 (2002). https://doi.org/10.1016/s0166-2236(02)02195-1

16 Paciotti, S., Bellomo, G., Gatticchi, L. & Parnetti, L. Are We Ready for Detecting alpha-Synuclein Prone to Aggregation in Patients? The Case of "Protein-Misfolding Cyclic Amplification" and "Real-Time Quaking-Induced Conversion" as Diagnostic Tools. *Front Neurol* **9**, 415 (2018). https://doi.org/10.3389/fneur.2018.00415

17 Concha-Marambio, L., Pritzkow, S., Shahnawaz, M., Farris, C. M. & Soto, C. Seed amplification assay for the detection of pathologic alpha-synuclein aggregates in cerebrospinal fluid. *Nat Protoc* **18**, 1179–1196 (2023). https://doi.org/10.1038/s41596-022-00787-3

18 Rossi, M. *et al.* Ultrasensitive RT-QuIC assay with high sensitivity and specificity for Lewy body-associated synucleinopathies. *Acta Neuropathol* **140**, 49–62 (2020). https://doi.org/10.1007/s00401-020-02160-8

19 Sorrentino, Z. A. *et al.* Physiological C-terminal truncation of alpha-synuclein potentiates the prion-like formation of pathological inclusions. *J Biol Chem* **293**, 18914–18932 (2018). https://doi.org/10.1074/jbc.RA118.005603

20 Ulamec, S. M. *et al.* Single residue modulators of amyloid formation in the N-terminal P1-region of alpha-synuclein. *Nat Commun* **13**, 4986 (2022). https://doi.org/10.1038/s41467-022-32687-1

21 Munishkina, L. A., Henriques, J., Uversky, V. N. & Fink, A. L. Role of protein-water interactions and electrostatics in alpha-synuclein fibril formation. *Biochemistry* **43**, 3289–3300 (2004). https://doi.org/10.1021/bi034938r

22 Metrick, M. A., 2nd *et al.* Million-fold sensitivity enhancement in proteopathic seed amplification assays for biospecimens by Hofmeister ion comparisons. *Proc Natl Acad Sci U S A* **116**, 23029–23039 (2019). https://doi.org/10.1073/pnas.1909322116

23 Giehm, L., Oliveira, C. L., Christiansen, G., Pedersen, J. S. & Otzen, D. E. SDS-induced fibrillation of alpha-synuclein: an alternative fibrillation pathway. *J Mol Biol* **401**, 115–133 (2010). https://doi.org/10.1016/j.jmb.2010.05.060

24 Giehm, L. & Otzen, D. E. Strategies to increase the reproducibility of protein fibrillization in plate reader assays. *Anal Biochem* **400**, 270–281 (2010). https://doi.org/10.1016/j.ab.2010.02.001

25 Orru, C. D. *et al.* Rapid and sensitive RT-QuIC detection of human Creutzfeldt-Jakob disease using cerebrospinal fluid. *mBio* **6** (2015). https://doi.org/10.1128/mBio.02451-14

26 Bhumkar, A. *et al.* Single-Molecule Counting Coupled to Rapid Amplification Enables Detection of alpha-Synuclein Aggregates in Cerebrospinal Fluid of Parkinson's Disease Patients. *Angew Chem Int Ed Engl* **60**, 11874–11883 (2021). https://doi.org/10.1002/anie.202014898

27 Ohgita, T., Namba, N., Kono, H., Shimanouchi, T. & Saito, H. Mechanisms of enhanced

526 aggregation and fibril formation of Parkinson's disease-related variants of alpha-
527 synuclein. *Sci Rep* **12**, 6770 (2022). https://doi.org/10.1038/s41598-022-10789-6

528 28 Lira, R. B., Steinkuhler, J., Knorr, R. L., Dimova, R. & Riske, K. A. Posing for a picture:
529 vesicle immobilization in agarose gel. *Sci Rep* **6**, 25254 (2016).
530 https://doi.org/10.1038/srep25254

531 29 Uemura, N. *et al.* alpha-Synuclein aggregates amplified from patient-derived Lewy
532 bodies recapitulate Lewy body diseases in mice. *Nat Commun* **14**, 6892 (2023).
533 https://doi.org/10.1038/s41467-023-42705-5

534 30 Luk, K. C. *et al.* Pathological alpha-synuclein transmission initiates Parkinson-like
535 neurodegeneration in nontransgenic mice. *Science* **338**, 949–953 (2012).
536 https://doi.org/10.1126/science.1227157

537 31 Tanriover, G. *et al.* Prominent microglial inclusions in transgenic mouse models of
538 alpha-synucleinopathy that are distinct from neuronal lesions. *Acta Neuropathol*
539 *Commun* **8**, 133 (2020). https://doi.org/10.1186/s40478-020-00993-8

540 32 Kumar, S. T. *et al.* How specific are the conformation-specific alpha-synuclein
541 antibodies? Characterization and validation of 16 alpha-synuclein conformation-specific
542 antibodies using well-characterized preparations of alpha-synuclein monomers, fibrils
543 and oligomers with distinct structures and morphology. *Neurobiol Dis* **146**, 105086
544 (2020). https://doi.org/10.1016/j.nbd.2020.105086

545 33 Soto, C. alpha-Synuclein seed amplification technology for Parkinson's disease and
546 related synucleinopathies. *Trends Biotechnol* **42**, 829–841 (2024).
547 https://doi.org/10.1016/j.tibtech.2024.01.007

548 34 Vascellari, S., Orru, C. D. & Caughey, B. Real-Time Quaking- Induced Conversion Assays
549 for Prion Diseases, Synucleinopathies, and Tauopathies. *Front Aging Neurosci* **14**,
550 853050 (2022). https://doi.org/10.3389/fnagi.2022.853050

551 35 Peng, C. *et al.* Cellular milieu imparts distinct pathological alpha-synuclein strains in
552 alpha-synucleinopathies. *Nature* **557**, 558–563 (2018). https://doi.org/10.1038/s41586-
553 018-0104-4

554 36 Peelaerts, W. *et al.* alpha-Synuclein strains cause distinct synucleinopathies after local
555 and systemic administration. *Nature* **522**, 340–344 (2015).
556 https://doi.org/10.1038/nature14547

557 37 Shahnawaz, M. *et al.* Discriminating alpha-synuclein strains in Parkinson's disease and
558 multiple system atrophy. *Nature* **578**, 273–277 (2020). https://doi.org/10.1038/s41586-
559 020-1984-7

560 38 Zhang, S. *et al.* Post-translational modifications of soluble alpha-synuclein regulate the
561 amplification of pathological alpha-synuclein. *Nat Neurosci* **26**, 213–225 (2023).
562 https://doi.org/10.1038/s41593-022-01239-7

563 39 Altay, M. F., Liu, A. K. L., Holton, J. L., Parkkinen, L. & Lashuel, H. A. Prominent astrocytic
564 alpha-synuclein pathology with unique post-translational modification signatures
565 unveiled across Lewy body disorders. *Acta Neuropathol Commun* **10**, 163 (2022).

https://doi.org/10.1186/s40478-022-01468-8

40 Okuzumi, A. *et al.* Propagative alpha-synuclein seeds as serum biomarkers for synucleinopathies. *Nat Med* **29**, 1448–1455 (2023). https://doi.org/10.1038/s41591-023-02358-9

41 Scialo, C. *et al.* TDP-43 real-time quaking induced conversion reaction optimization and detection of seeding activity in CSF of amyotrophic lateral sclerosis and frontotemporal dementia patients. *Brain Commun* **2**, fcaa142 (2020). https://doi.org/10.1093/braincomms/fcaa142

42 Kraus, A. *et al.* Seeding selectivity and ultrasensitive detection of tau aggregate conformers of Alzheimer disease. *Acta Neuropathol* **137**, 585–598 (2019). https://doi.org/10.1007/s00401-018-1947-3

43 Volpicelli-Daley, L. A., Luk, K. C. & Lee, V. M. Addition of exogenous alpha-synuclein preformed fibrils to primary neuronal cultures to seed recruitment of endogenous alpha-synuclein to Lewy body and Lewy neurite-like aggregates. *Nat Protoc* **9**, 2135–2146 (2014). https://doi.org/10.1038/nprot.2014.143

44 Mao, H. *et al.* Optimal Preservation of PFFs in Glycerol Enhances Suitability for Modeling Parkinson's Disease. *Small* **20**, e2401552 (2024). https://doi.org/10.1002/smll.202401552

45 Polinski, N. K. *et al.* Best Practices for Generating and Using Alpha-Synuclein Pre-Formed Fibrils to Model Parkinson's Disease in Rodents. *J Parkinsons Dis* **8**, 303–322 (2018). https://doi.org/10.3233/JPD-171248

Figure 1

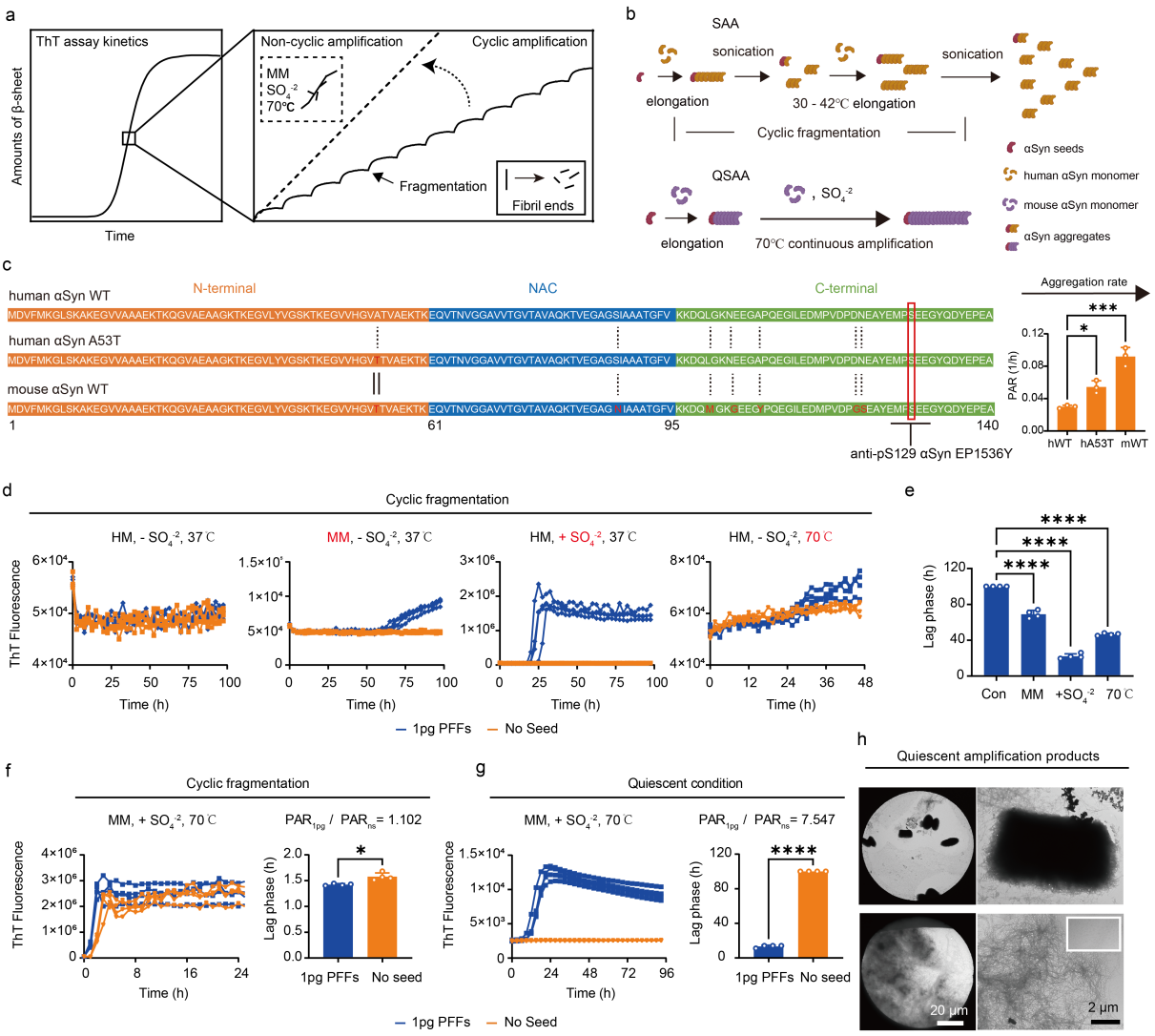

Fig. 1 | Development of a quiescent system for αSyn seed amplification. a, Schematic illustrating the kinetics of ThT assays. Conventional SAAs rely on cyclic fragmentation (solid line) to sustain rapid amplification. In each quiescent phase without fragmentation, elongation would typically plateau. In contrast, QSAA is designed to maintain continuous amplification under quiescent conditions (dashed line). **b,** Schematic comparing the mechanisms of SAA (cyclic fragmentation) and QSAA (quiescent amplification). **c,** Amino acid sequence alignment of human wild-type (hWT), human A53T, and mouse wild-type (mWT) αSyn. The bar chart quantifies the lag phase. **d,** ThT fluorescence kinetics of αSyn aggregation under cyclic fragmentation, assessing the effect of different monomers (MM),

599 sulfate ions (SO_4^{2-}), and temperature (70°C). Reactions were seeded with 1 pg of PFFs (blue)
600 or unseeded (orange). **e,** Quantification of the lag phase from experiments in **d**. **f-g,**
601 Aggregation kinetics and specificity under cyclic fragmentation (**f**) versus quiescent
602 conditions (**g**); bar charts show PAR (1 pg PFFs / no seed). **h,** Representative TEM images of
603 the fibrillar products generated by QSAA under optimized quiescent conditions. Insert,
604 unseeded control. Data are mean ± SD (n=3). *P < 0.05, ***P < 0.001, ****P < 0.0001; one-
605 way ANOVA with Tukey's post hoc test. Scale bars are indicated.

606

607 **Figure 2**

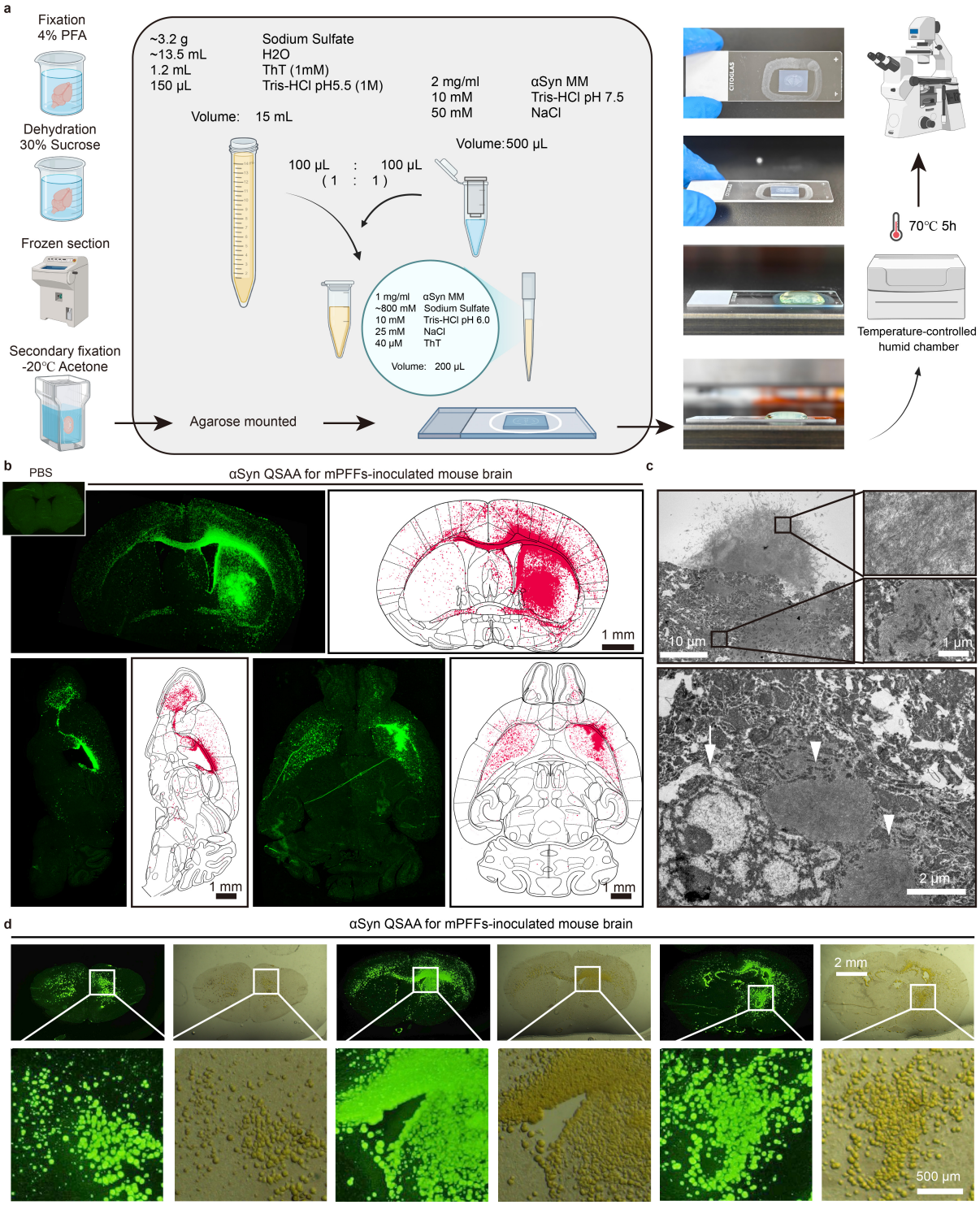

608

609 **Fig. 2 | QSAA enables in situ amplification and mapping of αSyn seeding activity in**

610 **mouse brain sections. a,** Schematic of the standardized operating procedure for in situ

611 QSAA on brain tissue, including tissue preparation, reagent preparation, and incubation on a

temperature-controlled stage with an agarose overlay. **b,** Representative images of in situ QSAA on coronal, sagittal, and horizontal sections from a mouse brain 180 dpi with mPFFs. Green fluorescence (ThT) indicates αSyn seeding activity. Corresponding anatomical atlas plates show the signal distribution (red dots). Inset: a PBS-injected control. **c,** TEM of a QSAA-treated tissue showing fibrillar structures; arrowheads indicate fibrils adjacent to nuclei. **d,** Coronal sections imaged by fluorescence and brightfield after QSAA incubation; macroscopic aggregates are shown alongside ThT signal. Images are representative of at least three independent experiments. Scale bars are indicated.

621 **Figure 3**

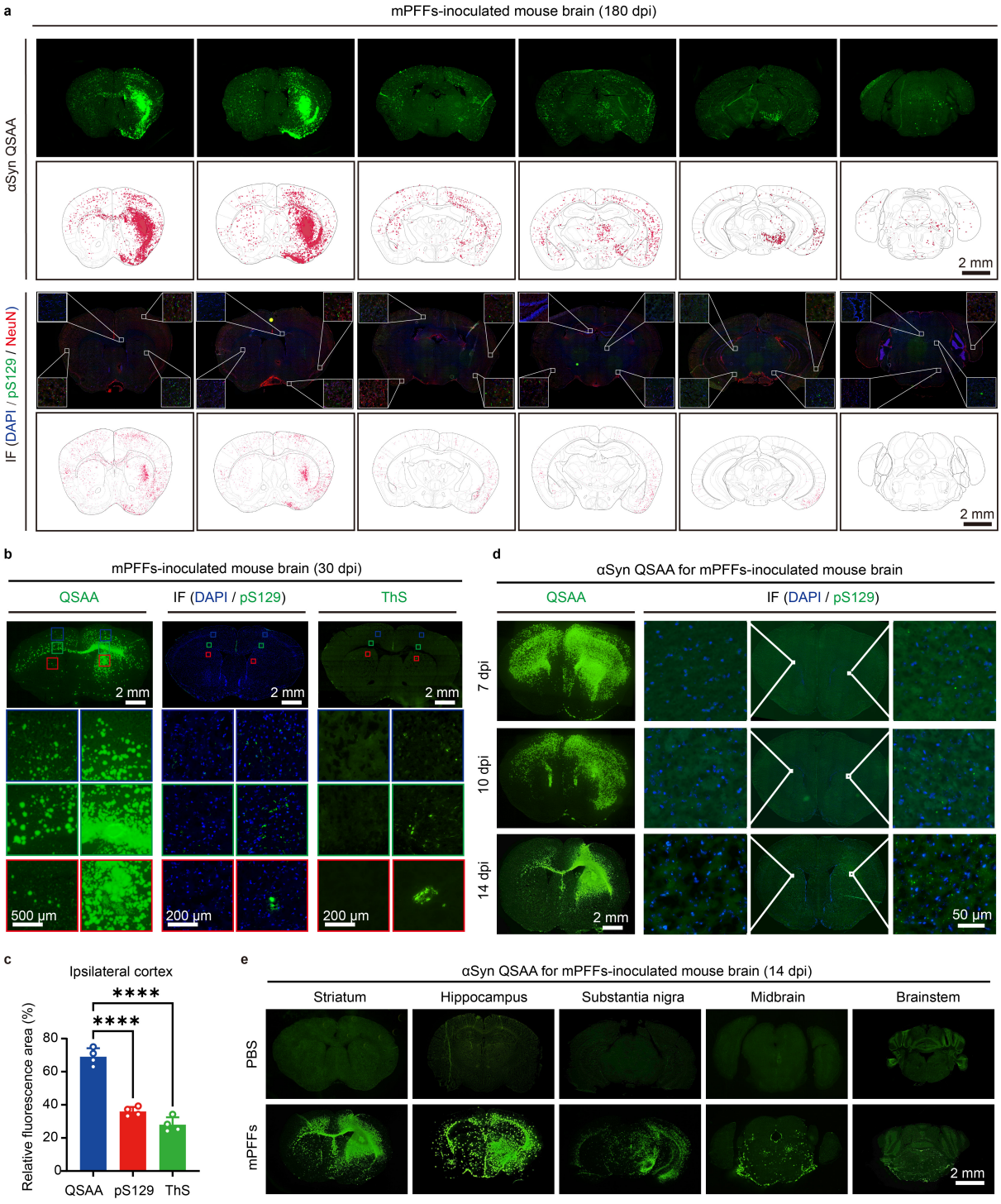

622

623 **Fig.3 | QSAA provides superior sensitivity and earlier detection of αSyn pathology in a**

624 **mouse model. a,** Brain-wide maps comparing the distribution of QSAA signal with pS129-IF

625 on consecutive sections from mPFF-injected mouse brain (180 dpi). **b,** Direct comparison of

626 QSAA, pS129-IF, and ThS staining on consecutive coronal sections from a mouse brain

injected with one-tenth the standard mPFFs dose and analyzed at 30 dpi. Colored boxes indicate magnified regions. **c,** Quantification of relative fluorescence units (RFU) from the cortical regions shown in **b**. Data are mean ± SD (n=3). **P < 0.01, ****P < 0.0001; one-way ANOVA with Tukey's post hoc test. **d,** Comparison of QSAA and pS129-IF in the mPFF-injected mouse model at 7, 10, and 14 dpi. **e,** Brain-wide map of αSyn seeding activity revealed by QSAA at 14 dpi in mPFF-injected mice compared to PBS-injected controls. Images are representative of at least three independent experiments. Scale bars are indicated.

Figure 4

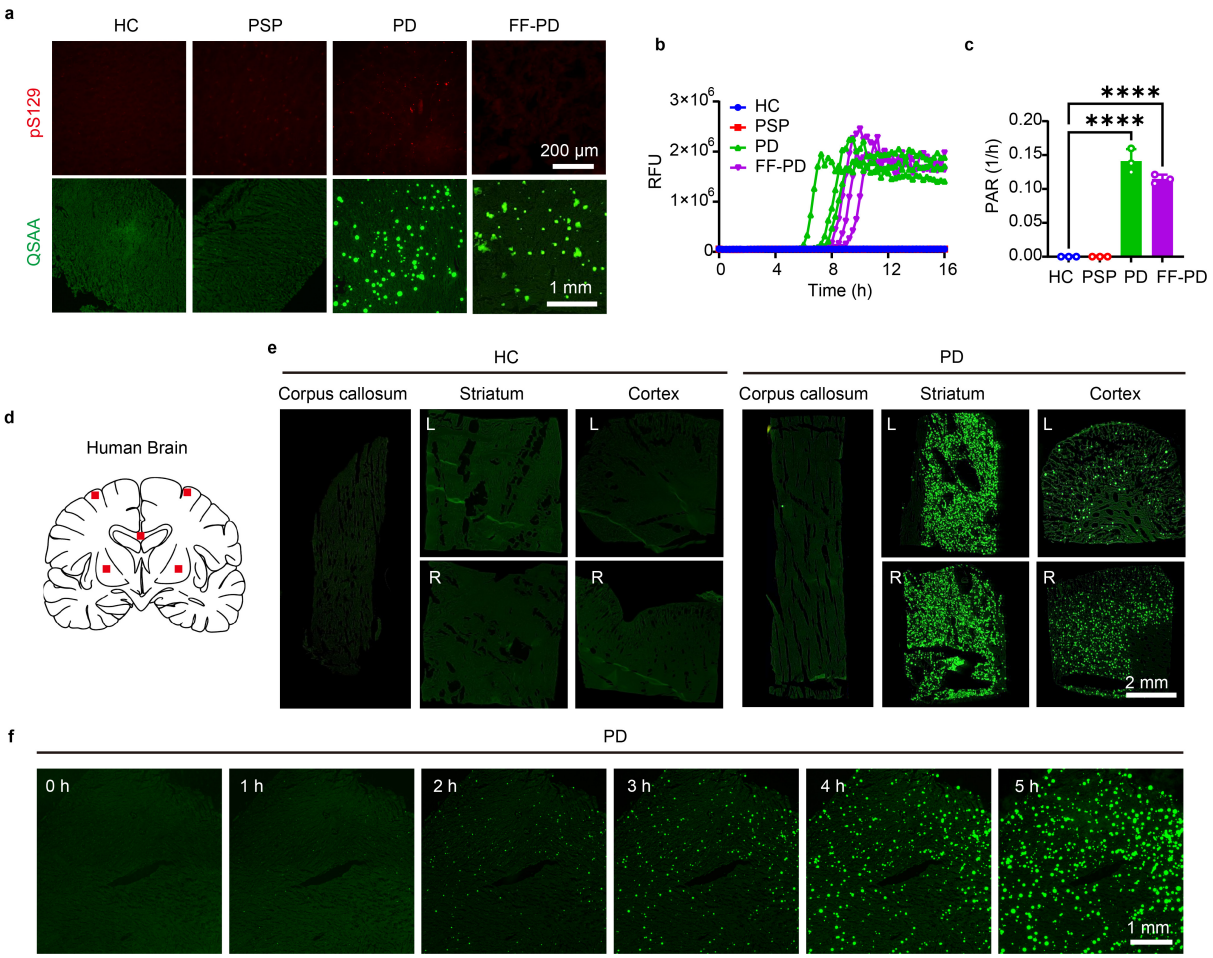

Fig. 4 | QSAA detects endogenous seeding activity in human postmortem brain tissue. a, Representative pS129-IF and QSAA results on striatal sections from HC, PSP, PD, and long-term formalin-fixed PD (>20 years; FF-PD). **b,** RT-QuIC of brain lysates from the same cases. **c,** Quantification of the PAR from RT-QuIC data in **b**. Data are mean ± SD (n=3). ****P < 0.0001; one-way ANOVA with Tukey's post hoc test. **d,** Schematic of brain section indicating the regions analyzed in **e**. **e,** Representative QSAA images of the corpus callosum, striatum, and cortex in HC and PD brains. L, left; R, right. **f,** Time-lapse QSAA imaging of a PD brain section during incubation (0-5 h). Scale bars are indicated.

Figure 5

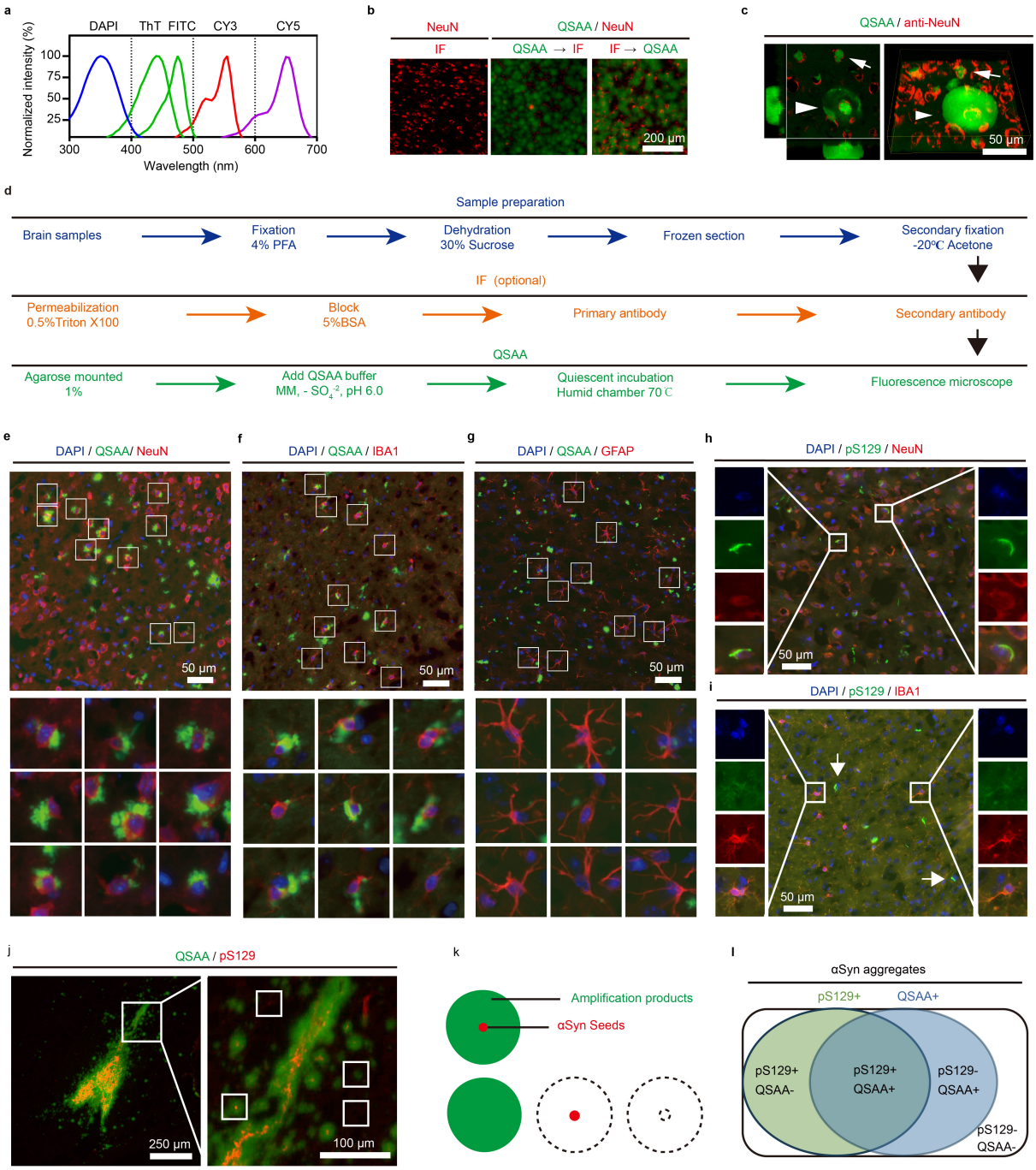

Fig. 5 | IF-QSAA reveals cellular localization of seeding activity and its relationship with pS129 pathology. a, Normalized excitation spectra of ThT and common fluorophores (DAPI, FITC, Cy3, Cy5). **b,** Workflow comparison showing QSAA-first versus IF-first sequence with NeuN staining. **c,** Confocal image of IF-QSAA on striatal sections from mPFF-inoculated mice (180 dpi) co-labeled for NeuN (red) and QSAA (green). Arrow and

653 arrowhead indicate selected cellular and extracellular structures. **d,** Schematic of the
654 optimized IF-QSAA protocol. **e, g,** IF-QSAA images of mPFF-injected mouse S2 cortex
655 sections (30 dpi) co-labeled with NeuN (**e**), IBA1 (**f**), and GFAP (**g**). Insets show magnified
656 cells. **h, i,** Consecutive S2 cortex sections (30 dpi) stained for pS129 and either NeuN (**h**) or
657 IBA1 (**i**); DAPI in blue. Arrows in **i** indicate selected pS129-positive neurons. **j,** High-
658 resolution image showing QSAA (green) with pS129 (red) in the mPFF-model at the injected
659 site. **k,** Schematic of core-halo arrangement of QSAA and pS129 signals in **j**. **l,** Conceptual
660 four-quadrant classification model of αSyn aggregates. Images are representative of at least
661 three independent experiments. Scale bars are indicated.

662

663 **Table 1: Key Reagents and Resources**

Reagent/Resource	Source	Catalog #	Application/Dilution
Antibodies			
Rabbit anti-pS129-αSyn	Abcam	ab51253	IF (1:1000)
Mouse anti-pS129-αSyn (clone 81A)	Abcam	ab184674	IF (1:1000)
Mouse anti-NeuN (clone A60)	Millipore	MAB377	IF (1:1000)
Rabbit anti-IBA1	FUJIFILM Wako	019-19741	IF (1:1000)
Mouse anti-GFAP	Cell Signaling Technology	3670	IF (1:1000)
Goat anti-Rabbit IgG (Alexa Fluor 488)	Invitrogen	A-11008	IF (1:1000)
Goat anti-Mouse IgG (Alexa Fluor 488)	Invitrogen	A-11001	IF (1:1000)
Goat anti-Rabbit IgG (Alexa Fluor 555)	Invitrogen	A-21428	IF (1:1000)
Goat anti-Mouse IgG (Alexa Fluor 555)	Invitrogen	A-21422	IF (1:1000)
Goat anti-Rabbit IgG (Alexa Fluor 647)	Invitrogen	A-21245	IF (1:1000)
Goat anti-Mouse IgG (Alexa Fluor 647)	Invitrogen	A-21235	IF (1:1000)
Chemicals, Buffers and Reagents			
Thioflavin T (ThT)	Sigma-Aldrich	T3516	40 μM (assays)
Thioflavin S (ThS)	Sigma-Aldrich	T1892	Staining
Na_2SO_4 (Sodium sulfate)	Sigma-Aldrich	238597	800 mM (QSAA buffer)

$(NH_4)_2SO_4$ (Ammonium sulfate)	Sigma-Aldrich	A4915	Purification
TureBlack Autofluorescence Quencher	Biotium	23007	Staining
Mineral oil	Biosharp	BS927	Overlay (quiescent SAA)
Protease inhibitor	Roche	04693116001	Protein expression/lysis
Endotoxin removal resin	Sangon Biotech	B641718	Endotoxin removal
Plastics and Consumables			
High-adhesion glass slides	CITOTEST	188105W	Section mounting
96-well black, clear-bottom plate	Nunc	165305	Agitated SAA
96-well PP PCR plate	Thermo Scientific	AB0700	Quiescent SAA
Optical adhesive film	Applied Biosystems	4311971	Plate sealing
HiTrap Q HP anion-exchange column	Cytiva	17115401	Protein purification
Amicon Ultra 50-kDa cutoff filter	Millipore	UFC905096	Filtration
10-µL Hamilton syringe, 33-g needle	Hamilton	65460-05	Stereotaxic injection
Instruments and Equipment			
Stereotaxic frame	Kopf Instruments	Model 940	Mouse surgery
ThermoMixer C	Eppendorf	5382	Fibril formation
Non-contact water-bath sonicator	SCIENTZ	SCIENTZ08-III	PFF fragmentation

Temperature-controlled stage	Ruicheng Instrument	TS400	In situ QSAA
Plate reader	Molecular Devices	SpectraMax iD5	ThT kinetics
Real-time PCR instrument	Bio-Rad	CFX96	Quiescent SAA
Plate reader (RT-QuIC)	BMG LABTECH	FLUOstar Omega	RT-QuIC
Inverted microscope	Nikon	ECLIPSE Ti2-E	Imaging
Confocal microscope	Leica Microsystems	SP8	Imaging
Transmission electron microscope	Thermo Fisher/FEI	Talos L120C	TEM
Software and Algorithms			
GraphPad Prism	GraphPad Software	v9.0	Statistics
Fiji/ImageJ	NIH	v2.3.0	Image analysis
NIS-Elements Advanced Research	Nikon	v5.30	Microscope image acquisition
Leica Application Suite X (LAS X)	Leica Microsystems	v3.5.7	Confocal image acquisition

664